Computers & Geosciences 174 (2023) 105311

Contents lists available at ScienceDirect

Computers and Geosciences

journal homepage: www.elsevier.com/locate/cageo

Grain boundary networks and shape preferred orientation – A fresh angle on pattern quantification with GBPaQ

Johanna Heeb [a,b,c,*], David Healy [b], Nicholas E. Timms [a], Enrique Gomez-Rivas [d]

[a] School of Earth and Planetary Sciences, Curtin University, Perth, WA, 6102, Australia
[b] School of Geosciences, King's College, University of Aberdeen, Aberdeen, AB24 3UE, United Kingdom
[c] Department of Earth Sciences, Faculty of Geosciences, Utrecht University, Utrecht, 3584 CB, the Netherlands
[d] Departament de Mineralogia, Petrologia i Geologia Aplicada, Facultat de Ciències de la Terra, Universitat de Barcelona, Martí i Franquès s/n, 08028, Barcelona, Spain

ARTICLE INFO

Keywords:
Shape preferred orientation
Intercept-based quantification
Grain boundary pattern symmetry
Strain evolution
GBPaQ toolbox

ABSTRACT

A quantitative understanding of grain shape preferred orientation (SPO) and grain boundary networks as fundamental characteristics of rocks and other crystalline solids is of major interest in geology and material science. Grain boundary networks contain useful information on the deformation history of polycrystalline aggregates, and their diagenetic and metamorphic histories. SPO can have a major impact on material characteristics such as permeability, acoustic velocity and mechanical strength, and on reaction surfaces. The objective of this study is to present a semi-automated toolbox of MATLAB™ scripts, named Grain Boundary Pattern Quantification (GBPaQ), that incorporate different methods for grain boundary pattern quantification for their application to, for example, seismic wave attenuation estimation. GBPaQ uses grain boundary statistics and calculates radial scan line intercepts. In this paper, GBPaQ is tested on two example grain boundary patterns, a granular texture and a foam texture with equant grains, which have been digitally stretched (deformed) to analyse their SPO evolution. The results show that a combination of grain ellipse, grain boundary segment orientation, and grain boundary segment intercept density rose diagrams provide a complete, detailed quantification of grain boundary pattern anisotropy. Grain boundary segment intercept (GBSI) analysis using GBPaQ yields a new grain boundary network parameter – the minimum intensity of grain boundary intercepts (I_{min}) – which follows a power law relationship with the average axial ratio of grain-fitted ellipses (r) during SPO development. We propose that I_{min} can be used for the quantitative analysis of SPO strength as a useful tool to assess the deformation history of polycrystalline aggregates. Further studies involving a broader range of different patterns and strain histories are necessary to fully investigate the potential of I_{min} versus r diagrams.

1. Introduction

Rock-forming grains and crystals are commonly non-equidimensional, leading to an aspect ratio > 1 (aspect ratio here is defined as the longest axis divided by the shortest axis). The shape of grains in rocks and crystalline materials is controlled by many factors, including the mineral habit and primary grain growth, deformation, recrystallisation, mineral reactions (e.g., diagenetic, metamorphic), and processes of erosion and transport of detrital grains. The shape preferred orientation (SPO) is generally defined as a measure of the alignment of non-equidimensional grains in a rock or crystalline material and is a fundamental descriptor of material microstructures and petrofabrics (Panozzo, 1984; Passchier and Trouw, 2005; Launeau et al., 2010). An SPO in a rock can be formed either during rock formation, e.g., by magmatic flow alignment of crystals or vesicles (Herrero-Bervera et al., 2001), by the alignment of particles during sediment deposition (Mulchrone and Meere, 2015), or as a consequence of deformation. SPOs are a common feature of many natural rocks, ceramics, and metals. As such, SPO quantification can provide useful information on the deformation history of polycrystalline aggregates, their diagenetic and metamorphic evolution, and the bulk strain field (Panozzo, 1987; Launeau and Robin, 1996; Berger et al., 2011). Furthermore, SPO can have a major impact on material characteristics, especially the anisotropy of mechanical and petrophysical properties, such as permeability, acoustic velocity, and mechanical strength.

The shape, size, and orientation arrangement of grains control the

* Corresponding author. Department of Earth Sciences, Faculty of Geosciences, Utrecht University, Utrecht, 3584 CB, the Netherlands.
E-mail address: j.heeb@uu.nl (J. Heeb).

https://doi.org/10.1016/j.cageo.2023.105311
Received 31 October 2021; Received in revised form 18 November 2022; Accepted 6 February 2023
Available online 14 February 2023

grain boundary microstructure. Given that grain boundaries are inherently weaker than grains, they can be transmissive to fluids, and can be sites of diffusion of vacancies, elements, and reactive transport (Urai et al., 2008). Accordingly, grain boundary networks exert a primary influence on the mechanical strength, permeability, and reactivity of a rock or material. The orientation of grain boundaries may also be used to define an SPO.

Grain boundary pattern quantification requires reliable resolution of grain boundaries via imaging (Launeau et al., 1990; Jähne, 1993; Bartozzi et al., 2000; Lebichot et al., 2005; Pirard and Sardini, 2011). A full description of an SPO should consider three dimensions because grains are 3D objects. However, our view of microstructures is often restricted to 2D surfaces, such as 2D outcrops and thin sections, and therefore SPO quantification techniques are most commonly developed for 2D analyses. While 3D methods are being developed (e.g., FIB-SEM etc.), and the results are very valuable, there is a "legacy database" of thousands of 2D thin sections and images. The take from this "legacy database" ought to be maximised. Manual recording (tracing) of different grain boundary patterns may take up to fifty times as long as digital processing and automated recording (Peternell and Kruhl, 2009; Kruhl, 2013).

The most established approaches to SPO quantification rely on the identification of grains, and other fabric objects such as xenoliths, clasts, or pebbles, as discrete objects (Webber, 2012), followed by the representation of their shapes as ellipses (in 2D) or ellipsoids (in 3D), which can be plotted on a Flinn plot (Flinn, 1962), a R_f/φ plot (Dunnet, 1969; Ramsay, 1976; Ramsay and Huber, 1983; Lisle, 1985), or as rose diagrams of grain long axis azimuths (in 2D). Moreover, the analysis of the positions of the ellipse centroids via the centre-to-centre method (Ramsay, 1976), its successor the Delaunay Triangulation Nearest Neighbour Method, and the Fry method (Fry, 1979) allow the finite strain ellipse (or ellipsoid in 3D) to be reconstructed (Sorby, 1849; Harker, 1885; Becker, 1893).

A hyperbolic vector mean method has been introduced to expand ellipse-based 2D strain analysis to incorporate hyperbolic (non-Euclidean) geometry (e.g., Yamaji, 2008, 2013a,b; Vollmer, 2018). This can be applied to data from, i.e., R_f/φ, centre-to-centre, and kinematic vorticity analysis. Equal area and gnomonic projections of the hyperboloid is demonstrably useful for estimating the optimal strain and its error by means of formal statistical methodology (e.g., Yamaji, 2008, 2013a,b; Vollmer, 2018).

Grain-based SPO approaches are recognised for being effective to derive principal strain axes from a population of deformed grains or objects, and are established tools for strain analysis (Webber, 2012; Kruhl, 2013). However, much information about the grain boundary network (pattern) is lost when grains are approximated as ellipses or in grain centroid approaches, highlighting the need for more sophisticated techniques for describing the geometry of grain boundary networks (or patterns) more thoroughly (Kruhl, 2013).

Methods for quantifying grain boundary patterns include those that analyse grain boundary attribute statistics, such as segment lengths and azimuths, and those that quantify grain boundary distribution statistics, such as intercepts along scan lines. Quantification of grain boundary segment orientation distributions (e.g., as grain boundary tensors) is advantageous because it does not rely on any geometric simplifications. A limitation of statistical analysis of the length and orientation of 'line elements' via cumulated frequency distributions (e.g., Sanderson, 1977; Sanderson and Phillips, 1987) is the loss of relationships of grain boundary segments relative to each other, grain size, and grain ellipticity (Kruhl, 2013). Grain boundary-based scan line quantification methods, such as the (inverse) SURFOR method of Panozzo (1983, 1984, 1987), the intercept method of Launeau and Robin (1996) or the Cantor-dust method (Volland and Kruhl, 2004), include more information about the shape and size of grains and pattern characteristics by analysing the relationship between the pattern and the scan line orientation. Scan lines allow a very detailed evaluation but are limited to the features in the pattern section that they capture (Kruhl, 2013).

The automated version of the SURFOR wheel from Panozzo (1984, 1987) has been implemented by the introduction of the SURFOR code (Heilbronner and Barret, 2014). This FORTRAN program was created to quantify fabrics defined by linear traces of grain surfaces from section images, and as such is ultimately a 2D limited tool. The SURFOR method has been used in hundreds of publications and has been applied to solve many geological problems (Herwegh et al., 1999; Molli and Heilbronner, 1999; Stipp et al., 2002; Kilian et al., 2011). These methods are commonly used to analyse SPO and strain in granites (Stein, 2000; Kurz, 2005; Vigneresse, 2015; Thabet et al., 2017), eclogites (Mauler et al., 2001; Pleuger et al., 2003; Kurz et al., 2004), mylonites (Stünitz and Gerald, 1993; Trullenque et al., 2006) and very common in marble and limestones (Schweigl and Neubauer, 1997; Molli et al., 2000; Cantisani et al., 2009). Some studies use the SURFOR approach to study hydration reactions (Marti et al., 2018a, 2018b).

The *intercept method* is one of the oldest methods for quantitative analysis of grain boundary pattern anisotropy (Launeau and Robin, 1996), was first suggested by Saltykov (1958), later used in stereology by Underwood (1970), and is based on counting intercepted grain boundary segments along parallel sets of scan lines that are rotated systematically. The number of boundaries that are intercepted along a scan line is called the intercept number. The most successful version of an intercept-based pattern quantification method was developed by Launeau and Robin (1996), following Launeau et al. (1990) and followed by Launeau and Robin (2005) and Launeau et al. (2010). Launeau and Robin (1996) added the Fourier analysis of intercept count to the intercept method. Fast Fourier Transform is part of autocorrelation and rose of intercept length (Launeau and Robin, 1996). A great advantage of this method is that direction-dependent pattern characteristics can be quantified, and this is especially important to link microstructures with the physical and mechanical behaviour of rocks in terms of seismic wave attenuation, deformation, or materials engineering.

Scan line-based methods are more selective because they utilize fragmented orientation and sectional results, depending on the position, angle, and length of scan lines. Information is lost by most scan line-based quantification approaches, because of the 10° angle between scan lines or the gaps between parallel scan lines in a grid. In general, scan line-based methods are strong for fast SPO quantification in simple patterns (Panozzo, 1983, 1984, 1987; Srivastava, 1995; Launeau and Robin, 1996).

The scan line and grain boundary-based quantification methods from Panozzo (1984, 1987) and Launeau and Robin (1996) are commonly applied to geological and other patterns for quantification analysis of finite strain and anisotropy, including seismic anisotropy (Lee and Jung, 2015; Jung et al., 2020; Kim and Jung, 2020). They are also applied to studies involving anisotropic magnetic susceptibility (Launeau and Cruden, 1998; Jayangondaperumal and Dubey, 2001).

The Cantor-Dust (or Cantor-Set) method was first proposed as a concept by Velde et al. (1990) and Harris et al. (1991). It is a method that combines boundary intercepts and grain size to describe a pattern. The method uses the distance between intercepts rather than the number of intercepts and is often used to analyse fractures or fracture spacing (Gerik and Kruhl, 2009). Volland and Kruhl (2004) modified the method for fractal pattern quantification and automated as the software tool AMOCADO by Gerik and Kruhl (2009).

Yet, published automated grain boundary pattern quantification software are limited by inherent simplifications in the approach that omit important details of the patterns. The specific aim of this study is to introduce GBPaQ, a new collection, or toolbox, of MATLAB™ programs, based on the code of FracPaQ – Fracture Pattern Quantification (Healy et al., 2017) for the automated quantitative analysis of grain boundary patterns. To illustrate and compare SPO quantification methods, two initial grain boundary patterns with narrow ranges in initial grain size distributions and low average axial ratios of grain-fitted ellipses (r) (Fig. 1a) were stretched, and the changes in SPOs tracked. GBPaQ requires vector graphic input. In this contribution we first introduce the

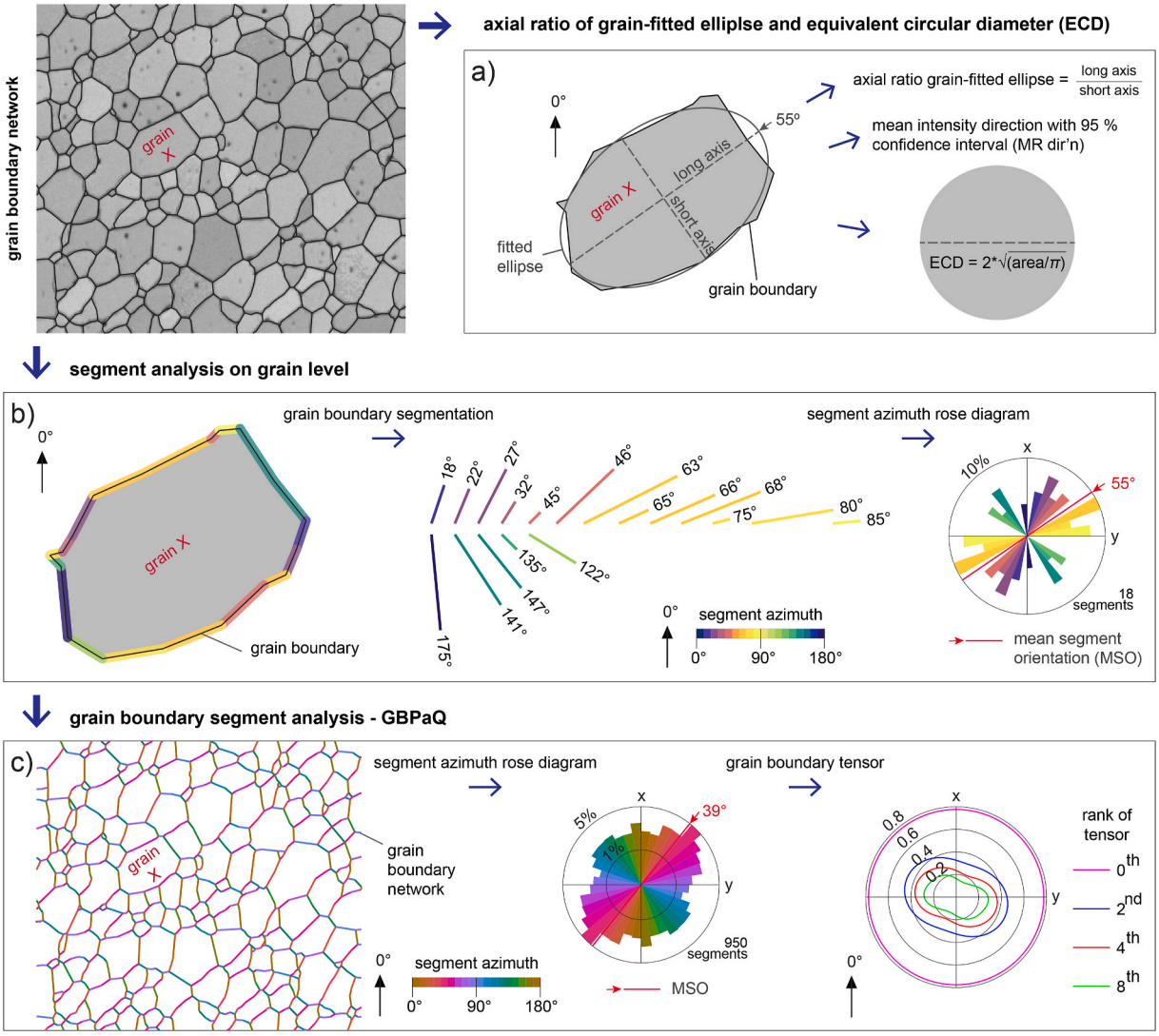

Fig. 1. Grain-based and grain boundary segment-based analytical methods used in the workflow of this study and explained using a grain boundary pattern section of a sintered zirconia ceramic sample ('Foam'). a) Established grain-based concepts used in approach one of the workflow, including grain-fitted ellipse-based analysis and equivalent circular diameter (ECD), explained on the example of one grain (grain x) of the sintered zirconia sample pattern. b) Grain boundary segment analysis explained by using the boundaries of grain x. c) Grain boundary segment analysis applied to the sample grain boundary network, and introduction of the grain boundary tensor.

GBPaQ approach and method and then demonstrate it using two different examples of grain boundary patterns.

2. Methods incorporated into GBPaQ

In this study, grain boundary patterns were analysed using three different approaches. The first approach is based on the fitted ellipse of grains (Fig. 1a), a widely recognised grain quantification method, and not incorporated into GBPaQ. The length and angle of the fitted ellipse longest grain axis and axial ratio of the longest and shortest axis of the fitted ellipse are calculated with freely available raster graphics software (ImageJ; Schneider et al., 2012). The mean intensity direction with 95% confidence interval (MR dir'n) was calculated from the long axis of the grain-fitted ellipses with GEOrient (Holcombe, 1998), an application designed to plot and analyse stereographic and equal area projections, and rose diagrams of geological structural data. The mean intensity is the direction of the resultant to the (unit) vectors describing the directions (Fischer, 1993; Mardia and Jupp, 2000). All directions are rounded to integer values and the mean resultant is given to the nearest integer direction. The 95% confidence interval of the mean direction is an estimate, based on the percentiles of the wrapped normal distribution using the circular standard error after Fischer (1993). The generated angles and rose diagrams are displayed counterclockwise with respect to the horizontal X, which corresponds to 0°. This was adjusted so that X is vertical, and a clockwise display of angles is used. The first approach consists of widely recognised methods and is not incorporated into GBPaQ. It is included into the workflow as part of the case study set up (i.e., problem specific).

The second approach to display the data is by showing azimuths and lengths of each grain boundary segment in a pattern using equal area rose plots generated by GBPaQ (Fig. 1b and c). The mean segment orientation (MSO) or circular mean is calculated for each pattern but is only truly valid for unimodal distributions. This grain boundary segment-based approach originates from fracture analysis and is built into the codes of GBPaQ (functionality) by using code from FracPaQ (Healy et al., 2017).

The third approach uses grain boundary segment intercepts (GBSIs) by scan lines to collect data on the orientation dependent GBSI densities of a grain boundary segment pattern. GBPaQ then generates GBSI density contour rose plots and identifies the average GBSI density $\overline{x}D_L(\theta)$,

the orientation and density of the minimum GBSI density α, and the maximum GBSI density γ. For this approach new code was developed and incorporated into GBPaQ.

2.1. Segment-based automated analysis

In this study, grain boundary patterns were analysed using a customised version of the MATLAB™ toolbox FracPaQ, originally designed to quantify fracture patterns (Healy et al., 2017), and renamed GBPaQ (**G**rain **B**oundary **Pa**ttern **Q**uantification). GBPaQ analysis consists of two parts, equivalent to the pre-described second and third approach of the workflow.

The first part is based on line statistics derived from coordinate geometry. Uploaded patterns are coloured for segment azimuth and a grain boundary tensor can be calculated (Fig. 1b and c). The output options include grain boundary length histograms, density maps, and orientation rose diagrams. Further, the patterns are entirely deconstructed, i.e., the grain boundary segments are removed from their spatial context, and the segment length and azimuth are statistically analysed and plotted as segment orientation rose diagrams (Fig. 1b and c). In GBPaQ, the analysis of the grain boundary segments by azimuth and the resulting rose diagram shows that the longest axis of the fitted ellipse and the vector that marks the circular mean, or mean segment orientation (MSO) have the same angle (Fig. 1a and b). Yet, the rose diagram captures more detailed pattern geometries compared to the grain-fitted ellipse-based approach (Fig. 1a and b), as it does not simplify the data and incorporates the nature of grains as unregular, non-elliptic shapes.

2.2. FracPaQ adaptations

The fracture pattern quantification toolbox FracPaQ was developed by Healy et al. (2017) to quantify digital 2D fracture patterns from thin section micrographs, geological maps, outcrop or aerial photographs, and satellite images. The source code is publicly available on GitHub™ and Mathworks™ FileExchange. It is built out of a suite of MATLAB™ scripts that incorporate previously published quantitative methods to analyse constituent fracture patterns in terms of their orientations, lengths, intensity, density, connectivity, and permeability. The implemented analytical methods are inherently scale independent and therefore applicable to micro- and up to macro-scales. Like for FracPaQ, two main types of input file data are accepted: tab-delimited ASCII text files of trace nodes ("node file") and graphical image files of traces ("image file"), for example SVG files. Like FracPaQ, GBPaQ builds a MATLAB™ **struct** array of traces (1 per segment in the input file), which consist of one or more segments delimited by *nodes*. Based on the node coordinates of each trace and each segment, lengths and orientations of the segments in the network are calculated. The quantification of lengths and orientations is reduced to simple operations of coordinate geometry. After loading the input file into the main plot window, output options can be selected on the right-hand side of the main window. When the applications are run, each selected map or plot is displayed in a separate figure window. The default length unit used is pixels. The produced maps and plots can be saved in various formats (e.g., pdf, jpeg, and png). Run time is strongly dependent on the number of traces in the input file. It can go from a few seconds to minutes.

GBPaQ simply repurposes the code and methods developed for quantification of fracture networks to quantify grain boundary attribute distributions and spatial variations based on the length and angle of line segments that comprise a grain boundary pattern. The output is then displayed as segment angle (azimuth) rose diagrams (Fig. 1b and c, middle), optionally length-weighted, and grain boundary (or fabric) 2nd, 4th and higher rank tensors (Fig. 1c, right side). Length-weighting of segments for segment azimuth rose diagrams gives weight to each bin by the total segment length that lies within that angular arc. Calculation of the tensor is based on the formulations of Oda (1983) (for applications see also Brown and Bruhn, 1998, and Suzuki et al., 1998). FracPaQ, uses a 2nd rank tensor approximation and calculates the anisotropy of permeability in 2D by default. GBPaQ uses the same approach and calculates fabric tensors using the density of segments (number per unit area), squared lengths of segments, and the orientation matrix of Woodcock (1977). The fabric tensor of a grain boundary pattern with an SPO will display inverse shape, and depending on the rank, more uniform shape compared to the grain boundary segment azimuth rose (Fig. 1c).

2.3. Grain boundary segment intercept-based automated analysis

The second, new part of GBPaQ and third part of the workflow is the grain boundary intercept-based analysis. GBPaQ in its current form has an automated radial centre setting (Fig. 2a, middle), so that it runs one rotation centre intercept analysis with 360 orientation steps per semicircle (interval between scan lines $d\beta = 0.5°$, adjustable). The GBSI density is calculated per pixel (adjustable to other units) and displayed as a GBSI density contour rose (equal area) (Fig. 2b). GBPaQ scan lines in this setting have constant length, defined by the smallest dimension of the input pattern image.

The average GBSI density $\overline{xD}$ is marked by a circular line on GBSI density rose diagrams (Fig. 2b). Values for intensity and azimuth of intercepts for maximum, minimum and average intercept number and density are annotated additionally. Further, two rose diagrams are generated that show azimuth and intensity of the grain boundary segments intercepted along the scan lines with the minimum and maximum intercept density (α and γ).

The basic concept of SPO analysis using scan lines is that a scan line parallel to the preferred grain elongation orientation of a pattern crosses less grain boundaries than in any other orientation. The distance between grain boundary segments depends, to a first order, on grain size, grain shape, grain boundary symmetry, the pattern geometry (sum of all grain boundary geometries in the pattern), and pattern homogeneity (grain size sorting, foliation domains, etc.). The presence of multiple phases and their specific differences in grain symmetries, sizes and shapes are also a factor for the characteristics of a grain boundary pattern. Grain size, intercept density and intensity variations are important in terms of the number of crossed segments: the more grains, the bigger the dataset, the more holistic the resulting description of a pattern, assuming it is homogeneous. Therefore, grain boundary pattern analysis should be conducted relative to grain size to analyse a statistically robust number of grains.

For grain boundaries described by a segment, length and angle are the key characteristics that need to be included in any method that attempts to quantify grain boundary-based pattern characteristics. A pattern with a well-defined SPO generally consists of long segments (or more numerous segments of equal lengths) parallel to the direction of the SPO, and shorter segments with increasing angular deviation from the SPO orientation (Fig. 3). This relationship gets more pronounced with increasing the SPO strength, visible by comparing Fig. 3a to b. It is statistically less likely to cross a short segment than a long one, with increasing angular difference (up to 90°) to the scan line. However, the likelihood of intercepting closely spaced grain boundary segments is increased normal to the SPO direction, which increases the intercept density in these scan line orientations (Fig. 3).

For any given analysis of a grain boundary pattern, the position and number of scan lines have a statistical impact and determine if the analysis describes a sample in 1D, 2D or 3D. A single scan line provides a 1D description of grain boundary density. Several parallel scan lines provide a 2D component to pattern quantification, but only describe the intercept density in one direction. The robust use of scan lines in 2D pattern analysis involves two concepts: a radial approach, where the scan lines rotate around a centre, and a grid approach, where a set of parallel scan lines is simultaneously rotated. The angle between scan lines in a centre approach and the angle increment of grid rotation matter in terms of the precision and scale at which the pattern is analysed.

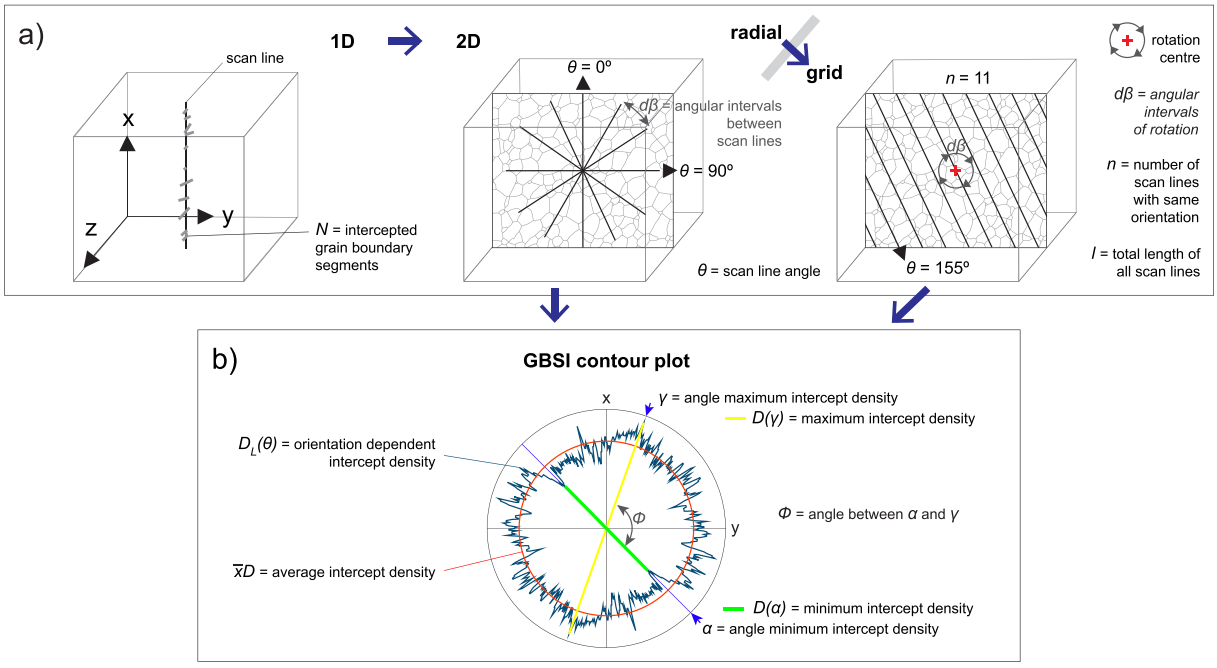

Fig. 2. Basic principles of grain boundary segment intercept (GBSI) analysis presented in this study. a) Progression from the one-dimensional placement of a scan line in a three-dimensional sample to two two-dimensional approaches, one with radial and the other, more data intense, with grid scan line distributions. b) Introduction of the GBSI density contour plot that describes the results from the radial and grid analysis.

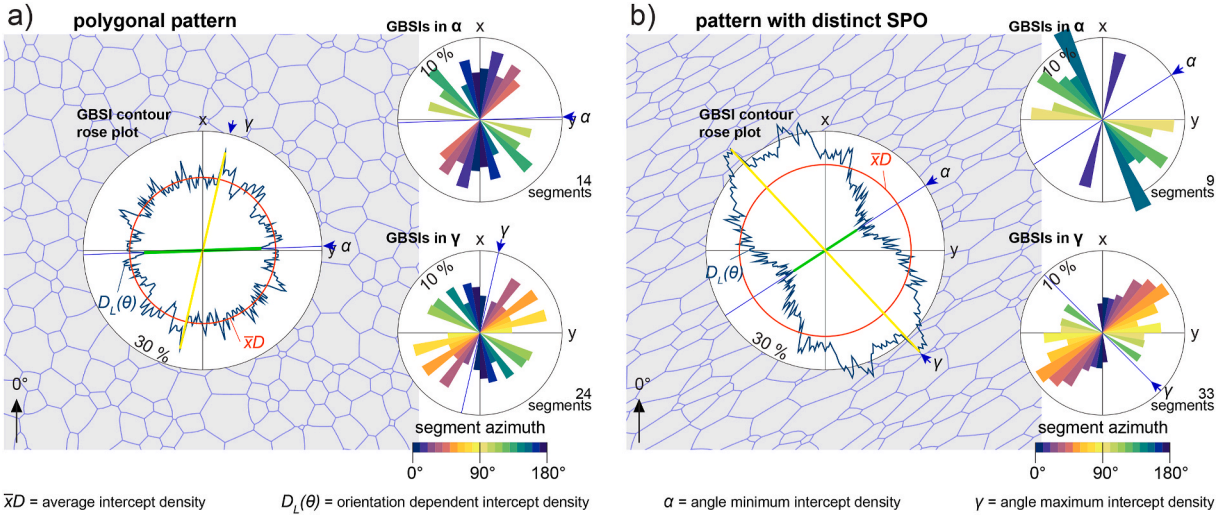

Fig. 3. Example for the influence of SPO on grain boundary segment lengths, distribution, and azimuths. a) GBSI-based analysis of a polygonal pattern, including a grain boundary segment map with GBSI density contour rose plot, and number and azimuths of the grain boundary segments intercepted along the scan lines in minimum and maximum GBSI density orientations (GBSIs in α and γ, length-weighted). b) GBSI-based analysis (equivalent to a) of a grain boundary segment pattern with distinct SPO, showing GBSI density contour development, growing difference in the number of grain boundary segments intercepted along α and γ, and an increased preferred orientation of segments intercepted along α and γ.

2.4. Calculations and metrics around grain boundary segment intercept analysis

The grain boundary segment intercept (GBSI) analysis using GBPaQ yields a new grain boundary network parameter – the minimum intensity of grain boundary intercepts (I_{min}). I_{min} can be useful for the quantitative analysis of SPO strength to assess the deformation history of polycrystalline aggregates. The minimum number of grain boundary segment intercepts (α) determined by GBPaQ GBSI analysis can be used to calculate the minimum intensity I_{min} (Eq. (1); Table 1), which relates the minimum number of grain boundary segment intercepts $N(\alpha)$ to the average number of grain boundary segment intercepts $\bar{x}N$. $\bar{x}N$ is the total number of intercepted grain boundary segments over all scan lines divided by the number of scan lines:

$$I_{min} = \frac{N(\alpha)}{\bar{x}N} \tag{1}$$

I_{min} as a rule ranges between 0 and 1, where 1 equals $\bar{x}N$, the average. The closer to 1, the weaker the SPO. With I_{min} decreasing towards 0, the SPO strength increases. This form of minimum intensity calculation requires that the length of all scan lines is equal. It can be adapted for multiple radial scan line centres and adjusted to intercept densities

Table 1
List of symbols and abbreviations used.

Symbol	Description
r	Average axial ratio of grain-fitted ellipses
N	Number of segment intercepts
θ	Scan line angle (between 0 and 180° from an arbitrary reference frame)
$d\beta$	Angular intervals between scan lines
n	Total number of scan lines with the same orientation
l	Total length of all scan lines
α	Orientation of scan line(s) with minimum segment intercept density
γ	Orientation of scan line(s) with maximum segment intercept density
φ	Angle between minimum and maximum segment intercept scan lines
$N(\alpha)$	Minimum number of segment intercepts
$N(\gamma)$	Maximum number of segment intercepts
$\bar{x}N$	Average number of segment intercepts (total number of intercepts divided by number of scan lines
$D_L(\theta)$	Orientation dependent segment intercept density (number of intercepts along one scan line orientation divided by scan line length of scan line(s) with this orientation)
$\bar{x}D_L(\theta)$	Average orientation dependent segment intercept density (grid approach)
$\bar{x}N_L(\theta)$	Average number of orientation dependent segment intercepts (grid approach)
$D_L(\alpha)$	Minimum segment intercept density
$D_L(\gamma)$	Maximum segment intercept density
I_{min}	Minimum intercept intensity

instead of number of intercepts.

The minimum intensity of grain boundary intercepts (I_{min}) as a new grain boundary network parameter was created with perspective to have a fast, dimensionless, and independent value useful to compare several patterns with different characteristics. I_{min} combines grain orientation distribution and elongation. Further, it is potentially sensitive to pattern attributes that are related to deformation mechanisms, non-equidimensional or rounded, elliptical grain shapes, and other characteristics of complex patterns. The full potential of I_{min} has yet to be evaluated.

The total number of GBSIs over multiple scan lines with the same orientation (θ) can be defined as $\sum_{i=1}^{n} N(\theta)_j$. The total number of scan lines in orientation θ is defined as n. $N(\theta)$ stands for the total number of GBSIs by one scan line with orientation θ. For the average number of GBSIs, the total number of GBSIs is divided by the total number of scan lines (constant length) used.

Extending the intercept analysis from a radial distribution of scan lines with a constant length to a radial distribution with different scan line lengths limited by the analysed map or collecting a higher data volume through a 'grid' scenario (Fig. 2a, right side) necessitates the calculation of GBSI densities instead of using absolute numbers of grain boundary segment intercepts. Especially for a 'grid' scenario, it is more efficient to use scan lines with different lengths to capture the whole grain boundary network. The total number of GBSIs of all scan lines in one orientation, $\sum_{i=1}^{n} N(\theta)$, is divided by the total length (l) of all scan lines ($\sum_{i=1}^{n} l_i$) with that orientation to calculate the total orientation-dependent grain boundary segment density $D_L(\theta)$:

$$D_L(\theta) = \frac{\sum_{i=1}^{n} N(\theta)}{\sum_{i=1}^{n} l_i} \tag{2}$$

The average number of orientation dependent GBSIs divided by scan line length of one scan line, under the condition that the scan line length is consistent, gives the average orientation dependent GBSI density $\bar{x}$ $D_L(\theta)$ for that orientation:

$$\bar{x}D_L(\theta) = \frac{\bar{x}N_L(\theta)}{l_{(\theta)}} \tag{3}$$

The list of symbols and abbreviations (Table 1) used and created for the new intercept-based analytical approach of this study is shown in Figs. 1–3 and further explanations of the mathematical basis for the GBSI minimum intensity and GBSI density are given to provide a basic understanding of the metrics used in this study.

3. Case studies

Two 2D grain boundary patterns have been selected as examples to illustrate grain boundary segment-based SPO quantification: a polycrystalline aggregate microstructure comprising grains with a high degree of roundness ('Granular') derived from an ELLE micro dynamic numerical model published in Piazolo et al. (2019), and a polycrystalline foam texture-based on an electron backscatter diffraction map of a sintered zirconia ceramic sample ('Foam'). The granular pattern was originally created to simulate trace element diffusion with fractionation during surface-energy driven grain boundary migration (Jessell et al., 2003; Steinbach et al., 2016; Llorens et al., 2019; Piazolo et al., 2019). It provides an example of a pattern with very low initial grain aspect ratios and minor variations in grain size distribution, whereas the grain shapes in 'Foam' are highly polygonal with relatively straight boundaries, minor variations in grain size, and homogeneous distribution (Table 1). Both patterns have very low variance in grain size, low SPO strength, relatively simple grain boundary patterns, and different grain shape symmetries. The patterns were mapped manually via a vector graphics program to create datasets in SVG file format for analysis with linear grain boundary line segments. The average equivalent circular diameter (ECD) and average axial ratio (r) were calculated from data analysis of these maps with ImageJ (see Table 2).

In order to study SPO evolution, grain boundary segment azimuths, and scan line intercept density, the two initial texture patterns were incrementally 'stretched' in the horizontal direction (using a vector graphics program) by 5%, 10%, and 50%, whereas the vertical dimension was held constant. These stretches do not simulate isochoric strain, as the area (and therefore volume in 3D) of the grains, and therefore the grain size, increases with progressive deformation. As such, these strains are analogous to x-y plane views of plane strain deformation.

4. Results

Results from combined analysis of the grain-fitted ellipse-based analysis with ImageJ and grain boundary segment azimuth analysis and GBSI-based analysis with GBPaQ show that the initial 'Granular' pattern does not preserve a SPO by all methods (Fig. 4a). The long axis grain-fitted ellipse orientation rose includes a maximum azimuth magnitude that covers 8.7% of the data at 38°, whereas grain boundary segment azimuth analysis shows a mean segment orientation (MSO) at 29° and the GBSI density-based α is 28.5°. Both grain boundary segment-based rose diagrams are uniformly rounded in shape overall.

The 'Foam' initial pattern (Fig. 4b) shows a stronger fitted ellipse long axis preferred orientation with the maximum azimuth magnitude of 12.2% and a well-defined 'neck' perpendicular to the maximum segment. The segment orientation rose has a distinct symmetry with a rhombic shape and bulging flanks. The shape of the GBSI density contour rose is almost hexagonal, with several maxima, and α at 135.5°. This is reflecting the polygonal character of the pattern and shows that the method is sensitive enough to capture pattern characteristics at this level of detail.

Incremental stretching of both initial patterns results in the systematic development of SPO (Fig. 4c and d). Throughout the progression, the maximum azimuth magnitude of the long axis orientation rose increases to 43% and 63.7% for 'Granular' and 'Foam' patterns,

Table 2
Selection criteria of the three primary patterns.

Sample	s	#grains	nECD±nSD	r±SD
'Granular'	5293	657	1±0.39	1.38±0.33
'Foam'	5925	953	1±0.50	1.59±0.50

s = number of segments in a pattern, #grains = number of whole grains per sample, nECD = equivalent circular diameter normalized to 1, nSD = normalized standard deviation, r = average grain axial ratio.

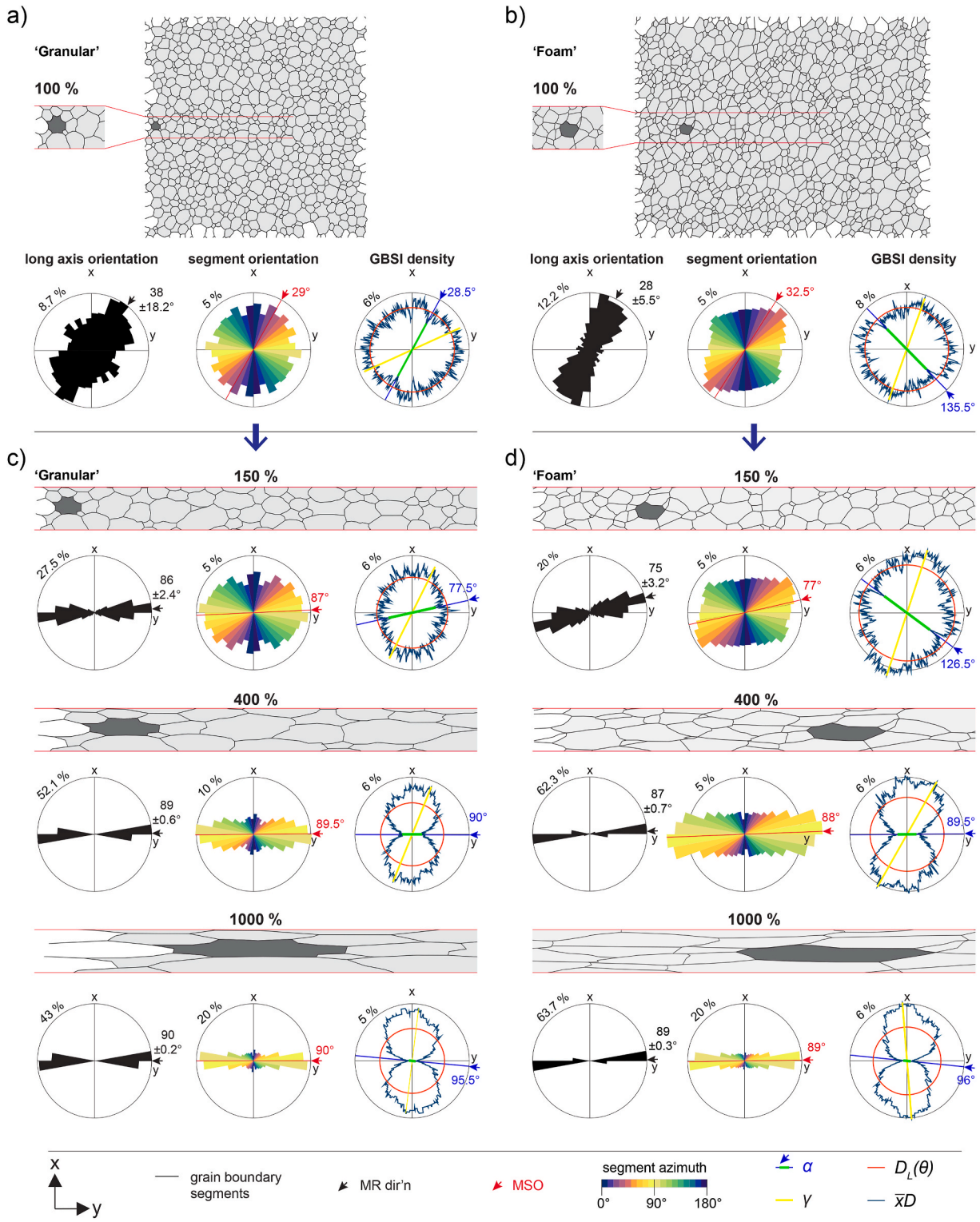

Fig. 4. Two case studies of 'simple' initial 2D grain microstructures: 'Granular' and 'Foam', analysed via three different analytical methods. a) and b) Analysis of original trace patterns of each microstructure with long axis orientation rose plots, based on the long axis of the fitted (grain) ellipses from ImageJ analysis data. Grains cut by the frame are excluded from the ImageJ analysis. The (grain boundary) segment orientation is plotted as equal area, non-length-weighted roses via GBPaQ. This dataset includes segments of rim grains. GBSI density contour rose diagrams from radial scan line distribution analysis. c) and d) Evolution of the patterns with stretching steps. A section of the grain boundary pattern with one grain marked throughout the stretching steps is shown for each selected step.

respectively, whereas the 95% confidence interval decreases from ±18.2° and ±5.5° to ±0.2° and ±0.3°. The segment orientation rose of 'Foam' reveals a rhombohedral shape until 400% stretch, with progressive thinning and elongation of the rhombus. The shape of the GBSI density rose for the 'Foam' pattern initially changes towards rhombic (at ~ 110–200% stretch), and then rapidly develops an 'hourglass shape' with α close to 90°, whereas the 'Granular' pattern forms the hourglass shape after ~ 250% stretch. This hourglass shape captures the

progression of SPO during horizontal incremental 'stretching' (plane strain deformation).

The value of length-weighting of the grain boundary segment azimuth data is tested by plotting the length-weighted and not length-weighted data of one input pattern into one rose and colouring the congruent sections (Fig. 5a). Length-weighting makes only a slight difference for the initial 'Granular' pattern with regular radial distribution of data in the grain boundary segment azimuth rose (Fig. 5a, top). Stretching of the 'Granular' pattern (150%) results in a rapid re-orientation of segment azimuths and length-weighting of the segments shows a more distinct effect with an increased range of azimuth magnitudes (Fig. 5a, middle). The non-length-weighted rose of the 'Foam' pattern (100%) has a very evenly rhombohedral shape, whereas the length-weighted rose shows that the maximum azimuth magnitude is surrounded by several similar intensity peaks (plateau) (Fig. 5a).

The direct comparison of the two approaches incorporated in GBPaQ, using a rose diagram at a stage where the pattern is undeformed (100%) or has a low level of deformation (150%) demonstrates how sensitive grain boundary segment azimuth and GBSI analysis are to the exact nature of the data (Fig. 5b). A regular radial distribution (Fig. 5b, top) with no obvious relation of local maxima and minima turns into a distinct inverse shape after 150% stretching for the 'Granular' case study (Fig. 5b, middle).

Plotting the GBSI density contour roses of all steps for the two patterns into a single rose diagram each further visualises that the density contours rapidly close in parallel to the orientation of stretching (Fig. 5c). Because the stretches do not simulate isochoric strain and strains are analogous to x-y plane views of plane strain deformation, the maximum GBSI density values, i.e., the top and bottom of the hourglass shape, do not change as rapidly and stay within a smaller range of magnitude compared to the minimum GBSI density values. Similar shape progression trends are visible for both case studies.

The grain boundary pattern evolution of the case studies is analysed by plotting the GBSI-based minimum intensity I_{min} against the average axial ratio of the grain-fitted ellipsoids r. The I_{min} development shows that I_{min} first decreases rapidly towards 0 with increasing stretching (Fig. 6a). Both grain boundary patterns have I_{min} trends that evolve following a general power function ($y = x^{-a}$) during stretching (Fig. 6b).

The variance of r, the standard error of the average axial ratio of grains in the grain boundary pattern, increases with increasing r because the range of the grain axial ratios increases due to the stretching. Grains that are initially more elongated and favourably oriented to the direction of stretching tend to become elongated more rapidly during the early steps. At the beginning of the evolution, with average axial ratios below 3 and I_{min} values above 0.55, the 'Granular' texture generally has higher I_{min} values compared to that of 'Foam'. Several identical values of I_{min} for increasing r are caused by limitations of the grain size in the grain boundary patterns. At a certain point of the analysis, the grain boundary density stays constant until the loss of a single GBSI causes a 'step' towards lower I_{min} that stays constant again until loss of another GBSI.

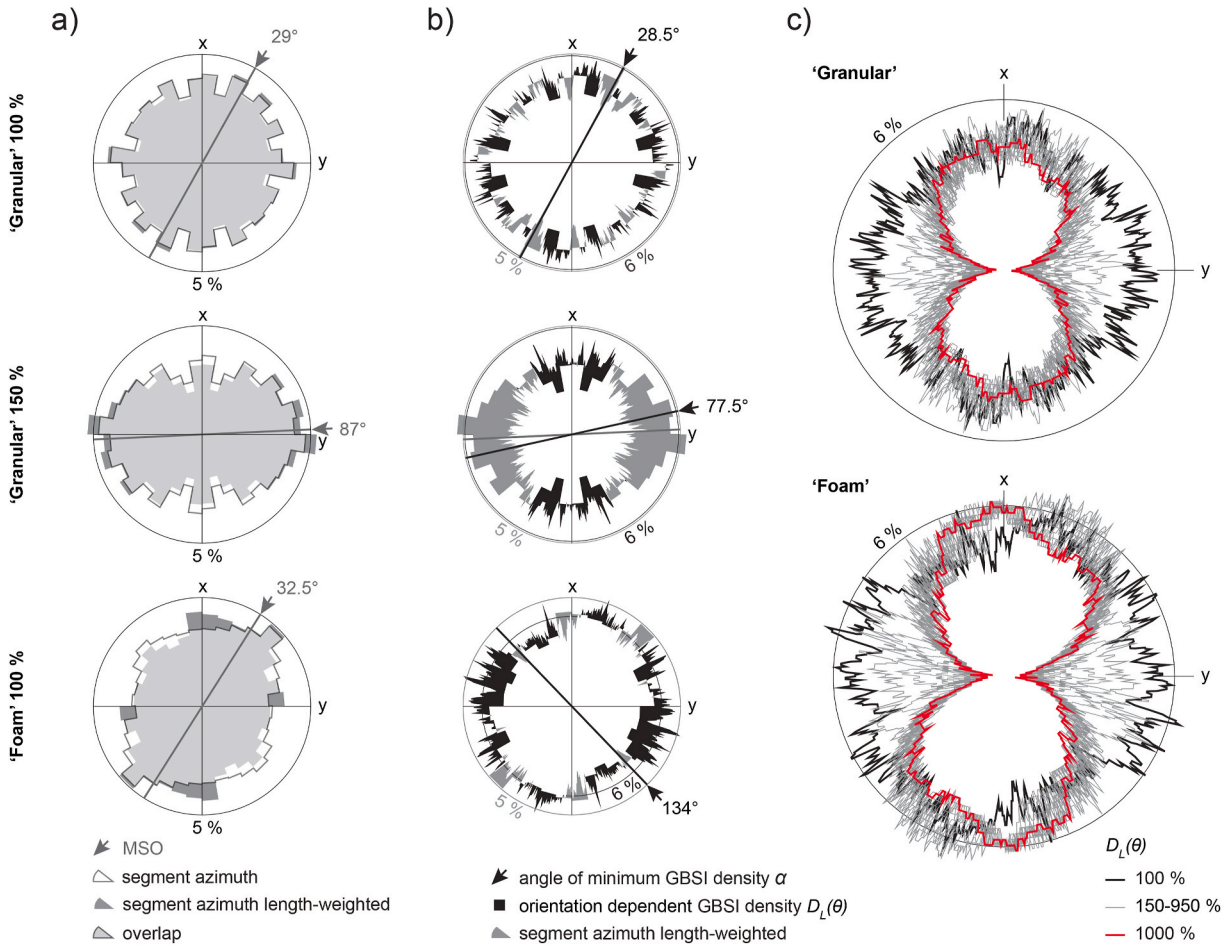

Fig. 5. Comparison of GBPaQ analytical methods of the 'Granular' and 'Foam' patterns at stages with no or weaker SPOs. a) Comparison of superimposed length-weighted and not length-weighted grain boundary segment orientation roses from GBPaQ analysis. b) Comparison of superimposed length-weighted segment orientation and GBSI density plots. c) Superimposed GBSI density contour rose diagrams of all stretching steps of the 'Granular' pattern and the 'Foam' grain boundary pattern.

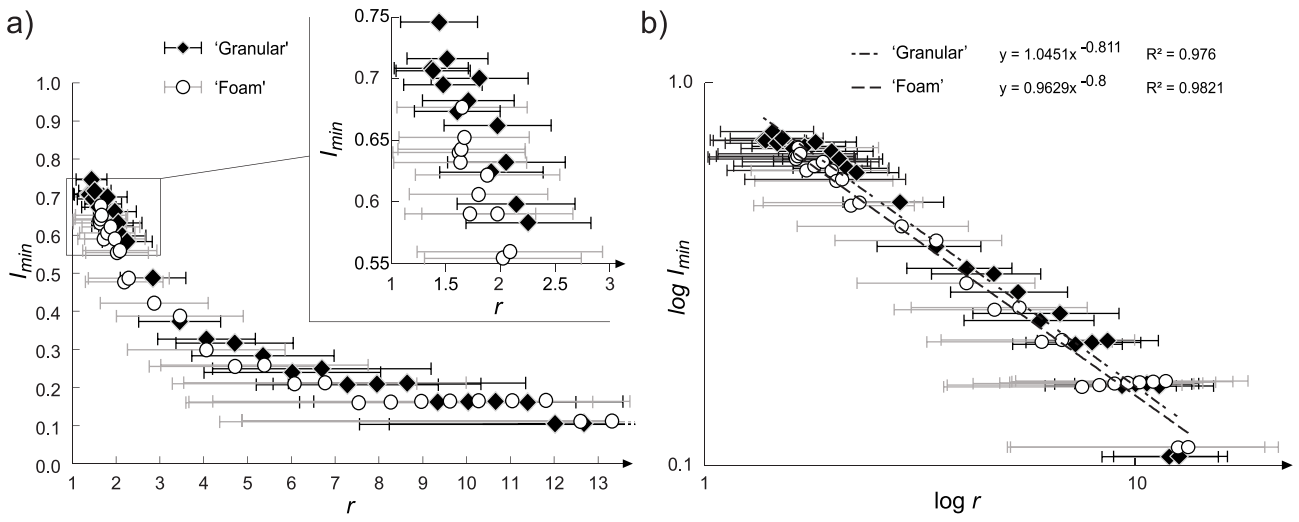

Fig. 6. Minimum intercept intensity I_{min} of the two patterns and stretching steps, plotted versus average axial ratio r of the fitted ellipse in a), and as power trend lines in log-log space in b).

5. Discussion

5.1. Comparison of the three approaches used

The long axis orientation (fitted ellipse), segment orientation, and GBSI density and orientation results of the 'Granular' pattern are perfectly consistent with each other (Fig. 4a,c). The 'Foam' pattern results show distinct deviations between the different methods (Fig. 4b,d). Whereas the long axis orientation and segment orientation roses are consistent at low stretch, GBSI density α is different by ~100°. Therefore, α is susceptible to subtle variations in the grain boundary pattern at low strains (weak SPOs) and does not necessarily coincide with the direction of stretching or orientation of the SPO.

The impact of length-weighting of grain boundary segments for segment azimuth analysis depends on the strength of the SPO and the grain shape (Figs. 4 and 5a). At low SPOs, this impact is small if the grain boundary segments describe highly rounded grains. If that is not the case, length-weighting of segments may provide additional information on the fabric, like features associated with a polygonal grain structure (Fig. 5a, bottom). However, the polygonal shape of the 'Foam' pattern translates better into the non-length-weighted rose, which is very evenly rhombohedral.

The mean intensity direction with 95% confidence interval (MR dir'n) of the long axis orientations of the grain-fitted ellipsoids and the circular mean segment orientation (MSO) of the grain boundary segment azimuths are based on the complete pattern, whereas the GBSI analysis without smoothing is selective (Figs. 1 and 2). Single radial scan results are susceptible to pattern inhomogeneity (i.e., stochastic variation), and are consequently sensitive to the position of the scan lines. GBPaQ does not have the option of applying the 'grid' scan line analysis yet. The distinct deviation of the density contour shape and angle α from GBSI density analysis, compared to results from the other methods (Fig. 4b,d) are a direct measure of inhomogeneity (stochastic fluctuations) in the grain boundary pattern rather than an 'uncertainty' due to imprecise quantification. The location of α depends on a single minimum value, which may be subject to such stochastic fluctuations in the grain boundary pattern. The application of a smoothing function could significantly reduce the impact of such stochastic fluctuations. However, the minimum GBSI density $D_L(\alpha)$ is a true measurement of the pattern and therefore a descriptor of a grain boundary pattern.

Contrary to conventional, more sophisticated strain analysis methods (e.g., Fry method, Delaunay Triangulation Nearest Neighbour Method), any smoothing algorithm needs to honour the complex shape of the GBSI density plots rather than smoothing these complex shapes to perfect ellipses. For example, some smoothing algorithms could easily eradicate GBSI minima and maxima, and therefore features like the rhombohedral GBSI density contour of the 'Foam' pattern would be lost. Therefore, it is necessary to evaluate the degree of necessary smoothing to allow for complex shapes.

5.2. Systematic evolution of I_{min} with increasing SPO strength

The grain boundary pattern evolution of the case studies is analysed by plotting the GBSI-based minimum intensity I_{min} against the average axial ratio of the grain-fitted ellipsoids r. I_{min} incorporates the grain elongation and the strength of preferred orientation of those elongated grains. When the SPO is weak, I_{min} is influenced by other factors like irregular grain shape characteristics. The average axial ratio r accounts for the grain elongation independent from the orientation of the grains relative to each other and is used as a measure of strain (stretch). Predictions of I_{min} from r or vice versa must be treated with caution, as the factors that influence I_{min} besides the SPO are not fully understood in terms of their relative impact. A tool for the identification and quantification of such factors would be useful.

The power law trend relationship of I_{min} and r (Fig. 6) is consistent with the simple geometrical consideration that the stronger the SPO, the greater the spacing between grain boundary segments in the maximum grain elongation alignment direction. Hence, stretching (strain) results in the rapid decrease of the number of GBSIs in α. This power law relationship is also visible in the GBSI density contour diagrams (Fig. 5c), where the contours at first rapidly (exponentially) close in parallel with the stretching orientation. The grain boundary segments get re-oriented and increase in length successively with increasing stretch. The concept of stretching is analogous to x-y plane views of plane strain deformation. The degree of this rotation during stretching is strongly dependent on the initial orientation and to a slightly lesser degree, on their length. Segments with closer azimuths to the direction of stretch rotate within the first increments of strain and lengthen more rapidly. The segments intercepted along α are selectively shorter and increasingly sorted for angles perpendicular to the orientation from the scan line with increasing SPO strength. In nature, formation of SPOs is of course often significantly more complex, but the basic concept of elongated grains and increased preferred orientation applies.

5.3. Potential applications of GBSI-based quantification to geological problems

The power law trend relation is a combination of two method approaches, as it combines the fitted ellipse-based r and the GBSI-based I_{min} concept. The calculation of the new network parameter I_{min} provides a tool for quantifying the SPO strength without being limited by scale or unit, and therefore makes it easy to compare a pattern to any other. The I_{min} versus r diagram with the definition of a reference power law trend makes it possible to plot any r or I_{min} and determine a range of the corresponding value. For the establishment of such a reference diagram, further investigations with different strain geometries and patterns with more complex geometry are inevitable. Further, the variance of I_{min} for patterns with low SPO (Fig. 6a) needs to be investigated. Identification and quantification of deformation mechanisms using a GBSI-based method in combination with quantitative grain boundary irregularity via sphericity parameter determination, as introduced by Fan et al. (2021), may be possible and of great value to determine what factors influence the GBSI density and I_{min}.

The big advantage of a GBSI approach is that pattern characteristics like the directional density of grain boundaries and grain pattern geometry are analysed directionally. Therefore, the GBSI rose plot can be used to study the impact of grain boundaries on directional characteristics like acoustic wave velocity anisotropy. Though it is known that seismic velocity is controlled to a high order by crystallographic preferred orientation (CPO) (e.g., Lloyd et al., 2011; Zhong et al., 2014; Vel et al., 2016), the impact of other petrofabrics like grain boundaries and SPO is not yet fully understood (e.g., Burlini and Kunze, 2000; Valcke et al., 2006; Vargas-Meleza et al., 2015).

Three possible main applications that involve GBSI-based quantification analysis via GBPaQ are identified, illustrating different strengths of this approach.

I) More representative pattern quantification combining fitted ellipse, segment geometry, and GBSI methods provides the opportunity of analysing more complex patterns than was possible before.
II) Comparative, quick (seconds to few minutes) SPO quantification of different, potentially unrelated grain boundary segment patterns by calculating I_{min} values, and with the potential to determine correspondent pattern characteristics using a future, more refined I_{min} versus strain diagram with reference power curve(s).
III) Direction-based grain boundary pattern quantification via GBSI density and orientation analysis provides more representative data on directional characteristics. GBPaQ could develop into a useful tool for studying the impact of grain boundary pattern inhomogeneity and anisotropy on rock characteristics like seismic wave attenuation, physical and mechanical behaviour. For this purpose, numerical models with pre-determined deformation parameters additional to analysing a range of well-known natural rock grain boundary patterns could be studied.

6. Conclusions

Given the established importance of grain boundary networks, it is critical that we quantify them with objective, robust, repeatable and open source methods. Accordingly, it is of major importance to quantify grain boundaries using state of the art automation (with toolboxes like GBPaQ) to support recent analytical developments (e.g., micro-CT). The minimum intercept intensity power law trend and GBSI density contour rose diagram are promising tools for further SPO and grain boundary pattern geometry quantification.

Testing of the GBSI approach on two different grain boundary patterns has led to the following findings.

- Length-weighting of segment orientation roses represents pattern geometry that may weaken SPO quantification but gives a more representative description of the grain boundary pattern without simplification.
- GBSI density roses capture a more representative depiction of directional characteristics of a grain boundary pattern, yet the orientations of α and γ are more likely to have big angular variations compared to non-GBSI-based methods, particularly in undeformed or weakly deformed samples. Higher angular variations in α and γ are anticipated for populations of approximately equant grains.
- Plotting the evolution of the GBSI minimum intensity I_{min} versus the average grain axial ratio r as data points shows a general trend that can be described by a power law.
- Further case studies involving numerical models and natural samples are necessary to further evaluate the value of I_{min} and the relation of this new grain boundary network parameter to strain.

Authorship contribution statement

Johanna Heeb: Substantial contribution to developed ideas, implementation, conception case studies, data acquisition, analysis, interpretation, drafting and critical revisiting of the manuscript, intellectual responsibility.

David Healy: Substantial contribution of developed ideas, implementation, coding and testing, drafting and critical revisiting of the manuscript, intellectual responsibility of its content. (advisor author).

Nicholas E. Timms: Substantial contribution of developed ideas, implementation, conception of case studies, drafting and critical revisiting of the manuscript, intellectual responsibility of its content. (advisor author).

Enrique Gomez-Rivas: Substantial contribution of developed ideas, implementation, drafting and critical revisiting of the manuscript, intellectual responsibility of its content. (advisor author).

Computer code availability

Name of code: GBPaQ.

Developer: David Healy, Johanna Heeb, Nicholas E. Timms, Enrique Gómez-Rivas E-Mail: d.healy@abdn.ac.uk.

Year first available: 2021.

Software required: MATLAB 2020

Program language: MATLAB.

Program size: 767 MB.

Source code: https://github.com/DaveHealy-github/GBPaQ.

Declaration of competing interest

The authors declare that they have no known competing financial interests or personal relationships that could have appeared to influence the work reported in this paper.

Data availability

The source code is available on GitHub. A link can be found in the 'Computer code availability' section of the publication.

Acknowledgements

The author acknowledges support from an Aberdeen-Curtin Alliance International Postgraduate Scholarship and a Curtin Publication Grant. The author thanks Chris Elders for supervision throughout this project, the PhD thesis examiners Thomas Blenkinsop, Steve Reddy, Mark Jessell, and Ian Alsop for their contributions to this work, the two referees, who gave valuable input for this publication, and Isabel Zutterkirch for helpful discussions. David Healy acknowledges funding from the UKRI NERC grant NE/T007826/1. Enrique Gomez-Rivas acknowledges the

"Ramón y Cajal" fellowship RYC2018-026335-I, funded by the Spanish Ministry of Science and Innovation (MCIN)/State Research Agency of Spain (AEI)/European Regional Development Fund (ERDF)/10.13039/501100011033, the DGICYT research project PID2020-585 118999GB-I00, funded by the Spanish Ministry of Science and Innovation (MCIN)/State Research Agency of Spain (AEI)/10.13039/501100011033, and the Grup Consolidat de Recerca "Geologia Sedimentària" (2021 SGR-Cat 00349), funded by the Catalan Council..

Appendix A. Supplementary data

Supplementary data to this article can be found online at https://doi.org/10.1016/j.cageo.2023.105311.

References

Bartozzi, M., Boyle, A.P., Prior, D.J., 2000. Automated grain boundary detection and classification in orientation contrast images. J. Struct. Geol. 22, 1569–1579. https://doi.org/10.1016/S0191-8141(00)00084-5.

Becker, G.F., 1893. Finite homogeneous strain, flow and rupture of rocks. Geol. Soc. Am. Bull. 4, 13–90. https://doi.org/10.1130/GSAB-4-13.

Berger, A., Herwegh, M., Schwarz, J.-O., Putlitz, B., 2011. Quantitative analysis of crystal/grain sizes and their distributions in 2D and 3D. J. Struct. Geol. 33, 1751–1763. https://doi.org/10.1016/j.jsg.2011.07.002.

Brown, S.R., Bruhn, R.L., 1998. Fluid permeability of deformable fracture networks. J. Geophys. Res. 103, 2489–2500. https://doi.org/10.1029/97JB03113.

Burlini, L., Kunze, K., 2000. Fabric and seismic properties of Carrara marble mylonite. Phys. Chem. Earth Solid Earth Geodes. 25, 133–139. https://doi.org/10.1016/S1464-1895(00)00022-3.

Cantisani, E., Pecchioni, E., Fratini, F., Garzonio, C.A., Malesani, P., Molli, G., 2009. Thermal stress in the Apuan marbles: relationship between microstructure and petrophysical characteristics. Int. J. Rock Mech. Min. Sci. 46, 128–137. https://doi.org/10.1016/j.ijrmms.2008.06.005.

Dunnet, D., 1969. A technique of finite strain analysis using elliptical particles. Tectonophysics 7, 117–136. https://doi.org/10.1016/0040-1951(69)90002-X.

Fan, S., Prior, D.J., Cross, A.J., Goldsby, D.L., Hager, T.F., Negrini, M., Qi, C., 2021. Using grain boundary irregularity to quantify dynamic recrystallization in ice. Acta Mater. 209, 1–22. https://doi.org/10.1016/j.actamat.2021.116810.

Fischer, N.I., 1993. Statistical Analysis of Circular Data. Cambridge University Press, UK, p. 277. Cambridge.

Flinn, D., 1962. On folding during three-dimensional progressive deformation. Quart. J. Geol. Soc. 118, 385–428. https://doi.org/10.1144/gsjgs.118.1.0385.

Fry, N., 1979. Random point distributions and strain measurement in rocks. Tectonophysics 60, 89–105. https://doi.org/10.1016/0040-1951(79)90135-5.

Gerik, A., Kruhl, J.H., 2009. Towards automated pattern quantification: time-efficient assessment of anisotropy of 2D patterns with AMOCADO. Comput. Geosci. 35, 1087–1097. https://doi.org/10.1016/j.cageo.2008.01.015.

Harker, A., 1885. On slaty cleavage and allied rock structures with special reference to the mechanical theories of their origin. In: Report of the 55th Meeting of the British Association for the Advancement of Science, pp. 813–852.

Harris, C., Franssen, R., Loosveld, R., 1991. Fractal analysis of fractures in rocks: the Cantor's Dust method-comment. Tectonophysics 198, 107–111. https://doi.org/10.1016/0040-1951(91)90135-F.

Healy, D., Rizzo, R.E., Cornwell, D.G., Farrell, N.J.C., Watkins, H., Timms, N.E., et al., 2017. FracPaQ: a MATLAB™ toolbox for the quantification of fracture patterns. J. Struct. Geol. 95, 1–16. https://doi.org/10.1016/j.jsg.2016.12.003.

Heilbronner, R., Barret, S., 2014. Image analysis in earth sciences. Microstruct. Text. Earth Mater. 283–303.

Herrero-Bervera, E., Walker, G.P.L., Cañon-Tapia, E., Garcia, M.O., 2001. Magnetic fabric and inferred flow direction of dikes, conesheets and sill swarms, Isle of Skye, Scotland. J. Volcanol. Geoth. Res. 106, 195–210. https://doi.org/10.1016/S0377-0273(00)00293-6.

Herwegh, M., Handy, M.R., Heilbronner, R., 1999. Evolution of mylonitic microfabrics (EMM), a computer application for educational purposes. Tectonophysics 303, 141–146. https://doi.org/10.1016/S0040-1951(98)00252-2.

Holcombe, R., 1998. GEOrient plots stereographic projections and rose diagrams [Program]. available. http://www.earthsciences.uq.edu.au/;rodh/software/, 6 November1998.

Jähne, B., 1993. Digital image processing: concepts, algorithms, and scientific applications. https://doi.org/10.1007/978-3-662-21817-4.

Jayangondaperumal, R., Dubey, A.K., 2001. Superposed folding of a blind thrust and formation of klippen: results of anisotropic magnetic susceptibility studies from the Lesser Himalaya. J. Asian Earth Sci. 19, 713–725. https://doi.org/10.1016/S1367-9120(00)00066-3.

Jessell, M.W., Kostenko, O., Jamtveit, B., 2003. The preservation potential of microstructures during static grain growth. J. Metamorph. Geol. 21, 481–491. https://doi.org/10.1046/j.1525-1314.2003.00455.x.

Jung, S., Jung, H., Austrheim, H., 2020. Microstructural evolution of amphibole peridotites in åheim, Norway, and the implications for seismic anisotropy in the mantle wedge. Minerals 10 (345), 1–22. https://doi.org/10.3390/min10040345.

Kilian, R., Heilbronner, R., Stünitz, H., 2011. Quartz microstructures and crystallographic preferred orientation: which shear sense do they indicate? J. Struct. Geol. 33, 1446–1466. https://doi.org/10.1016/j.jsg.2011.08.005.

Kim, J., Jung, H., 2020. Lattice preferred orientation (LPO) and seismic anisotropy of amphibole in gapyeong amphibolites. Korean J. Mineral. Petrol. 33, 259–272. https://doi.org/10.22807/KJMP.2020.33.3.259.

Kruhl, J.H., 2013. Fractal-geometry techniques in the quantification of complex rock structures: a special view on scaling regimes, inhomogeneity and anisotropy. J. Struct. Geol. 46, 2–21. https://doi.org/10.1016/j.jsg.2012.10.002.

Kurz, W., 2005. Constriction during exhumation: evidence from eclogite microstructures. Tectonophysics 33, 37–40. https://doi.org/10.1130/G20887.1.

Kurz, W., Jansen, E., Hundenborn, R., Pleuger, J., Schäfer, W., Unzog, W., 2004. Microstructures and crystallographic preferred orientations of omphacite in Alpine eclogites: implications for the exhumation of (ultra-) high-pressure units. J. Geodyn. 37, 1–55. https://doi.org/10.1016/j.jog.2003.10.001.

Launeau, P., Bouchez, J.-L., Benn, K., 1990. Shape preferred orientation of object populations: automatic analysis of digitized images. Tectonophysics 180, 201–211. https://doi.org/10.1016/0040-1951(90)90308-U.

Launeau, P., Cruden, A.R., 1998. Magmatic fabric acquisition mechanisms in a syenite: results of a combined anisotropy of magnetic susceptibility and image analysis study. J. Geophys. Res. Solid Earth 103, 5067–5089. https://doi.org/10.1029/97JB02670.

Launeau, P., Robin, P.-Y.F., 1996. Fabric analysis using the intercept method. Tectonophysics 267, 91–119. https://doi.org/10.1016/S0040-1951(96)00091-1.

Launeau, P., Robin, P.-Y.F., 2005. Determination of fabric and strain ellipsoids from measured sectional ellipses—implementation and applications. J. Struct. Geol. 27, 2223–2233. https://doi.org/10.1016/j.jsg.2005.08.003.

Launeau, P., Archanjo, C.J., Picard, D., Arbaret, L., Robin, P.-Y., 2010. Two- and three-dimensional shape fabric analysis by the intercept method in grey levels. Tectonophysics 492, 230–239. https://doi.org/10.1016/j.tecto.2010.06.00.

Lebichot, S., Dislaire, G., Pirard, E., Launeau, P., 2005. Grey level intercepts distributions and grain size estimation. In: Proceedings. 8th International Congress on Stereology and Image Analysis, Zakopane, Poland, pp. 102–110.

Lee, J., Jung, H., 2015. Lattice-preferred orientation of olivine found in diamond-bearing garnet peridotites in Finsch, South Africa and implications for seismic anisotropy. J. Struct. Geol. 70, 12–22. https://doi.org/10.1016/j.jsg.2014.10.015.

Lisle, R.J., 1985. Geological Strain Analysis: A Manual for the Rf/ϕ Technique. Pergamon, London.

Llorens, M.-G., Gomez-Rivas, E., Ganzhorn, A.-C., Griera, A., Steinbach, F., Roessiger, J., et al., 2019. The effect of dynamic recrystallisation on the rheology and microstructures of partially molten rocks. J. Struct. Geol. 118, 224–235. https://doi.org/10.1016/j.jsg.2018.10.013.

Lloyd, G.E., Butler, R.W.H., Casey, M., Tatham, D.J., Mainprice, D., 2011. Constraints on the seismic properties of the middle and lower continental crust. Geol. Soc., London, Special Publ. 360, 7–32. https://doi.org/10.1144/SP360.2.

Mardia, K.V., Jupp, P.E., 2000. Directional Statistics. John Wiley and Sons, London, p. 464.

Marti, S., Stünitz, H., Heilbronner, R., Plümper, O., Kilian, R., 2018a. Syn-kinematic hydration reactions, dissolution-precipitation creep and grain boundary sliding in experimentally deformed plagioclase-pyroxene mixtures. Solid Earth Discuss. 1–40. https://doi.org/10.5194/se-2018-39.

Marti, S., Stünitz, H., Heilbronner, R., Plümper, O., Kilian, R., 2018b. Syn-kinematic hydration reactions, grain size reduction, and dissolution–precipitation creep in experimentally deformed plagioclase–pyroxene mixtures. Solid Earth 9, 985–1009. https://doi.org/10.5194/se-9-985-2018.

Mauler, A., Godard, G., Kunze, K., 2001. Crystallographic fabrics of omphacite, rutile and quartz in Vendée eclogites (Armorican Massif, France). Consequences for deformation mechanisms and regimes. Tectonophysics 342, 81–112. https://doi.org/10.1016/S0040-1951(01)00157-3.

Molli, G., Heilbronner, R., 1999. Microstructures associated with static and dynamic recrystallization of Carrara marble (Alpi Aquane, NW Tuscany, Italy). Geol. Mijnbouw 78, 119–126. https://doi.org/10.1023/A:1003826904858.

Molli, G., Conti, P., Giorgetti, G., Meccheri, M., Oesterling, N., 2000. Microfabric study on the deformational and thermal history of the Alpi Apuane marbles (Carrara marbles), Italy. J. Struct. Geol. 22, 1809–1825. https://doi.org/10.1016/S0191-8141(00)00086-9.

Mulchrone, K.F., Meere, P.A., 2015. Shape fabric development in rigid clast populations under pure shear: the influence of no-slip versus slip boundary conditions. Tectonophysics 659, 63–69. https://doi.org/10.1016/j.tecto.2015.08.003.

Oda, M., 1983. A method for evaluating the effect of crack geometry on the mechanical behaviour of cracked rock masses. Mech. Mater. 2, 163–171. https://doi.org/10.1016/0167-6636(83)90035-2.

Panozzo, R., 1984. Two-dimensional strain from the orientation of lines in a plane. J. Struct. Geol. 6, 215–221. https://doi.org/10.1016/0191-8141(84)90098-1.

Panozzo, R., 1987. Two-dimensional strain determination by the inverse SURFOR wheel. J. Struct. Geol. 9, 115–119. https://doi.org/10.1016/0191-8141(87)90049-6.

Panozzo, R.H., 1983. Two-dimensional analysis of shape-fabric using projections of digitized lines in a plane. Tectonophysics 95, 279–294. https://doi.org/10.1016/0040-1951(83)90073-2.

Passchier, C.W., Trouw, R.A.J., 2005. Microtectonics. In: Revised and Enlarged Edition, 2nd. Springer-Verlag Berlin Heidelberg, Berlin, Heidelberg, pp. 102–109.

Peternell, M., Kruhl, J.H., 2009. Automation of pattern recognition and fractal-geometry-based pattern quantification, exemplified by mineral-phase distribution patterns in igneous rocks. Comput. Geosci. 35, 1415–1426. https://doi.org/10.1016/j.cageo.2008.11.001.

Piazolo, S., Bons, P.D., Griera, A., Llorens, M.-G., Gomez-Rivas, E., Koehn, D., et al., 2019. A review of numerical modelling of the dynamics of microstructural

development in rocks and ice: past, present and future. J. Struct. Geol. 125, 111–123. https://doi.org/10.1016/j.jsg.2018.05.025.
Pirard, E., Sardini, P., 2011. Image analysis for advanced characterization of industrial minerals and geomaterials. EMU Notes in Mineralogy 9, 287–340. https://doi.org/10.1180/EMU-notes.9.3.
Pleuger, J., Hundenborn, R., Kremer, K., Babinka, S., Kurz, W., Jansen, E., Froitzheim, N., 2003. Structural evolution of the Adula nappe, Misox zone, and Tambo nappe in the San Bernardino area: constraints for the exhumation of the Adula eclogites. Mittl. Osterreichischen Geol. Ges. 94, 99–122 ([in German]).
Ramsay, J.G., 1976. Folding and Fracturing of Rocks. McGraw-Hill, International series in the earth and planetary sciences, New York [etc, p. 568 [7th print.
Ramsay, J.G., Huber, M.I., 1983. Strain Analysis. The Techniques of Modern Structural Geology, vol. 1. Academic Press, London (v-xii s).
Saltykov, S.A., 1958. Stereometric Metallography, second ed. State Publishing House for Metals Sciences, Metallurgizdat, Moscow, p. 446.
Sanderson, D.J., 1977. The analysis of finite strain using lines with an initial random orientation. Tectonophysics 43, 199–211. https://doi.org/10.1016/0040-1951(77)90117-2.
Sanderson, D.J., Phillips, S.J.L., 1987. Strain analysis using length-weighting of deformed random line elements. J. Struct. Geol. 9, 511–514. https://doi.org/10.1016/0191-8141(87)90129-5.
Schneider, C.A., Rasband, W.S., Eliceiri, K.W., 2012. NIH Image to ImageJ: 25 years of image analysis. Nat. Methods 9, 671–675. https://doi.org/10.1038/nmeth.2089.
Schweigl, J., Neubauer, F., 1997. Semiductile deformation in pelagic limestones at diagenetic conditions. Geol. Carpathica 48, 361–370.
Sorby, H.C., 1849. On the origin of slaty cleavage. Proc. Yorks. Geol. Soc. 3, 300–312. https://doi.org/10.1144/pygs.3.300.
Srivastava, H.B., 1995. Two-dimensional strain estimation from weakly deformed rocks. Ann. Tect. 9, 3–6.
Stein, E., 2000. Zur Platznahme von Granitoiden: vergleichende Fallstudien zu Gefügen und Platznahmemechanismen aus den White-Inyo Mountains, California, USA, und dem Bergsträsser Odenwald = on the emplacement of granitoids case studies comparing fabrics and emplacement mechanisms of the White-Inyo Mountains, California, USA, and the Bergsträsser Odenwald, Germany. Stuttgart, E. Schweizerbart'sche Verlagsbuchhandlung. Geotekt. Forsch. 93, 344 ([in German]).
Steinbach, F., Bons, P.D., Griera, A., Jansen, D., Llorens, M.-G., Roessiger, J., Weikusat, I., 2016. Strain localization and dynamic recrystallization in the ice–air aggregate: a numerical study. Cryosphere 10, 3071–3089. https://doi.org/10.5194/tc-10-3071-2016.
Stipp, M., Stünitz, H., Heilbronner, R., Schmid, S.M., 2002. The eastern Tonale fault zone: a 'natural laboratory' for crystal plastic deformation of quartz over a temperature range from 250 to 700°C. J. Struct. Geol. 24, 1861–1884. https://doi.org/10.1016/S0191-8141(02)00035-4.
Stünitz, H., Gerald, J.D.F., 1993. Deformation of granitoids at low metamorphic grade. II: granular flow in albite-rich mylonites. Tectonophysics 221, 299–324. https://doi.org/10.1016/0040-1951(93)90164-F.
Suzuki, K., Oda, M., Yamazaki, M., Kuwahara, T., 1998. Permeability changes in granite with crack growth during immersion in hot water. Int. J. Rock Mech. Min. Sci. 35, 907–921. https://doi.org/10.1016/S0148-9062(98)00016-3.
Thabet, I., Kilias, A., Kamh, S., 2017. Microstructural finite strain analysis of the Hafafit granitoids domes South Central Eastern desert of Egypt. Bull. Geol. Soc. Greece 47, 667. https://doi.org/10.12681/bgsg.11100.
Trullenque, G., Kunze, K., Heilbronner, R., Stünitz, H., Schmid, S.M., 2006. Microfabrics of calcite ultramylonites as records of coaxial and non-coaxial deformation kinematics: examples from the Rocher de l'Yret shear zone (Western Alps). Tectonophysics 424, 69–97. https://doi.org/10.1016/j.tecto.2006.06.004.
Underwood, E.E., 1970. Quantitative Stereology. Addison-Wesley Publishing, Menlo Park, Reading, MA, p. 274.
Urai, J.L., Schléder, Z., Spiers, C.J., Kulka, P.A., 2008. Flow and transport properties of salt rocks. In: Dynamics of Complex Intracontinental Basins. The Central European Basin System, pp. 277–290. https://doi.org/10.1007/978-3-540-85085-4.
Valcke, S., Casey, M., Lloyd, G., Kendall, J.-M., Fisher, Q., 2006. Lattice preferred orientation and seismic anisotropy in sedimentary rocks. Geophys. J. Int. 166, 652–666. https://doi.org/10.1111/j.1365-246X.2006.02987.x.
Vargas-Meleza, L., Healy, D., Alsop, G.I., Timms, N.E., 2015. Exploring the relative contribution of mineralogy and CPO to the seismic velocity anisotropy of evaporites. J. Struct. Geol. 70, 39–55. https://doi.org/10.1016/j.jsg.2014.11.001.
Vel, S.S., Cook, A.C., Johnson, S.E., Gerbi, C., 2016. Computational homogenization and micromechanical analysis of textured polycrystalline materials. Comput. Methods Appl. Mech. Eng. 310, 749–779. https://doi.org/10.1016/j.cma.2016.07.037.
Velde, B., Dubois, J., Touchard, G., Badri, A., 1990. Fractal analysis of fractures in rocks: the Cantor's Dust method. Tectonophysics 179, 345–352. https://doi.org/10.1016/0040-1951(90)90300-W.
Vigneresse, J.-L., 2015. Textures and melt-crystal-gas interactions in granites. Geosci. Front. 6, 635–663. https://doi.org/10.1016/j.gsf.2014.12.004.
Volland, S., Kruhl, J.H., 2004. Anisotropy quantification: the application of fractal geometry methods on tectonic fracture patterns of a Hercynian fault zone in NW Sardinia. J. Struct. Geol. 26, 1499–1510. https://doi.org/10.1016/j.jsg.2003.10.005.
Vollmer, F.W., 2018. Automatic contouring of geologic fabric and finite strain data on the unit hyperboloid. Comput. Geosci. 115, 134–142. https://doi.org/10.1016/j.cageo.2018.03.006.
Webber, J.R., 2012. Dissertations and Theses. Advances in Rock Fabric Quantification and the Reconstruction of Progressive Dike Replacement in the Coastal Batholith of Central Chile, vol. 238. Graduate College. https://scholarworks.uvm.edu/graddis/238.
Woodcock, N.H., 1977. Specification of fabric shapes using an eigenvalue method. Geol. Soc. Am. Bull. 88, 1231–1236. https://doi.org/10.1130/0016-7606(1977)88%3C1231:SOFSUA%3E2.0.CO;2.
Yamaji, A., 2008. Theories of strain analysis from shape fabrics: a perspective using hyperbolic geometry. J. Struct. Geol. 30, 1451–1465. https://doi.org/10.1016/j.jsg.2008.07.011.
Yamaji, A., 2013a. Comparison of methods of algebraic strain estimation from Rf/ϕ data: a unified theory of 2D strain analysis. J. Struct. Geol. 49, 4–12. https://doi.org/10.1016/j.jsg.2013.01.011.
Yamaji, A., 2013b. Two-dimensional finite deformations evaluated from pre- and post-deformation markers: application to balanced cross sections. J. Struct. Geol. 51, 144–155. https://doi.org/10.1016/j.jsg.2013.02.002.
Zhong, X., Frehner, M., Kunze, K., Zappone, A., 2014. A novel EBSD-based finite-element wave propagation model for investigating seismic anisotropy: application to Finero Peridotite, Ivrea-Verbano Zone, Northern Italy. Geophys. Res. Lett. 41, 7105–7114. https://doi.org/10.1002/2014GL060490.